Buckling deformation of polymer electrolyte membrane and membrane electrode assembly under humidity cycles

Tomoaki Uchiyama *, Manabu Kato, Toshihiko Yoshida

Toyota Motor Corporation, Fuel Cell System Development Div., R&D Group 2, 1200, Mishuku, Susono, Shizuoka 410-1193, Japan

ABSTRACT

Wrinkle deformations of both a polymer electrolyte membrane (PEM) and a membrane electrode assembly (MEA) under humidity cycles were analyzed. The NRE211 and NRE212 of commercial Nafion® were the PEMs used in this study. The MEA was composed of NRE212 and catalyst layers (CLs) between gas diffusion layers (GDLs) in a single cell and was exposed to 10 humidity cycles. The MEA deformed into a wrinkle shape at a width ranging between 330 and 500 μm. The compressive stress of the MEA under swelling was calculated using the MEA swelling ratio and Young's modulus, while the critical stress for the buckling of the MEA was estimated with Euler's in-plane buckling theory. By comparing these stresses, it was concluded that the MEA buckled under swelling. Moreover, the deformations of PEMs and MEAs against microscopic circular clearances under humidity cycles were analyzed. Both showed bulge deformations at clearances above each specific diameter, which can be estimated by the Euler in-plane buckling theory. Required PEM properties for preventing buckling are lower swelling ratios in the in-plane direction and thicker membranes. Additionally, a flat surface on the GDL is effective in preventing buckling. Preventing MEA buckling enables the long-term utilization of fuel cells.

1. Introduction

In researching methods to increase the durability of polymer electrolyte membrane (PEM) fuel cells (FCs) for automobiles, many challenges have been faced over several decades. The durability of the materials composing the FC is important; performance drops are caused by chemical and electrochemical degradations of a catalyst layer (CL). The phenomenon of PEM degradation has also been reported in chemical damage [1] and mechanical damage cases [1–3]. As PEM damage would create pinholes leading to a gas crossover, the investigation of the PEM degradation phenomena is essential, especially investigations of mechanical degradation, which, compared to chemical degradation research, are quite limited. The study examples used include a failure mode analysis [1–3], a stress/strain analysis using the finite element method (FEM) [4–10] and a life prediction of the PEM [3,11–13] and membrane electrode assembly (MEA) [3,14]. The understanding of PEM and MEA behaviors under the FC usage environments contributes to the mechanical design based on the life prediction.

Large PEM swelling contributes to good proton conductivity for large power generation in FCs. The swelling of the PEM is caused by the absorption of water produced by an electrochemi-

cal reaction in the cathode, CL. Alternatively, the PEM shrinks via desorption of water with a decrease in humidity in FCs. Water absorption/desorption behaviors lead to a stress change in the PEM [4–10]. Over a long duration, the PEM undergoes deformation and becomes thinner than its initial state. The cracks in the CLs are verified as well [1,2]. Eventually, pinholes, by breaking off of the PEM, cause an increase in the gas permeation [1–3]. It is known that CL cracks are formed during the CL manufacturing process [15], in humidity cycles by a repeated expansion and shrinkage of the PEM [1,2] and in severe conditions like freeze/thaw cycles [16,17]. These CL cracks could affect the PEM deformation.

However, the mechanism for the mechanical degradation of the MEA under humidity cycles has not been verified. The wrinkle deformation of the MEA, caused by the compressive stress along with the in-plane swelling of the MEA (Fig. 1), as an initial phase of the degradation has not been discussed thus far. The zero or low fastening force from gas flow fields to the MEA contributes to the wrinkle deformation. This lower fastening force is confirmed within channel portions at grooved gas flow fields [4–6,10] and at GDL surfaces with imperfect geometry [18,19]. The PEM swells by water absorption, and the thickness will increase at a narrow clearance at the interface between the MEA and GDL (Fig. 2(a)). On the contrary, wide clearance at the interface may lead to in-plane buckling of the MEA (Fig. 2(b)).

Research data on wrinkle deformation is insufficient, and there remains a wide, unexplored domain. The present research aims to obtain more fundamental knowledge in order to design the

* Corresponding author. Tel.: +81 55 997 9078; fax: +81 55 997 7120.
E-mail address: tomoaki@uchiyama.tec.toyota.co.jp (T. Uchiyama).

(1) Initial condition
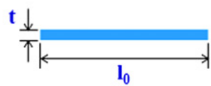
(2) In-plane swelling without edge constrain

ε : swelling strain
$= (l_1 - l_0) / l_0$

(3) In-plane swelling with edge constrain

t: thickness
2a: membrane buckling diameter

Compressive stress (Swelling stress) > Critical stress for buckling

Fig. 1. MEA wrinkle in a circular plate under swelling.

MEA and GDL on the basis of the MEA deformation mechanism. The present paper will first report the data obtained from the experiments conducted, demonstrating the PEM and MEA wrinkle deformations under humidity cycles. The wrinkle mechanism is explained by the Euler in-plane buckling theory. The focus then moves to MEA buckling in several circular clearances, imitating the clearance between the MEA and GDL. The purpose of this task is to reveal the relationship between the clearances and the MEA properties and to furnish the design data for the MEA and GDL. The circular microscopic holes fabricated in polyimide films were used to investigate PEM and MEA buckling under humidity cycles. The minimum diameter causing in-plane buckling in PEMs and MEAs with different thicknesses and in-plane swelling ratios were considered.

2. Experimental procedures

2.1. Materials

Commercial NRE211 and NRE212 (DuPont, USA) in acid form were used in all experiments. The NRE211 (26 μm thickness) and NRE212 (52 μm thickness) are cast homogeneous perfluorosulfonic acid membranes with the trade name Nafion® [7,9–11,13,28,29]. Their equivalent weight (EW) is 1100 g mol^{-1}. Nafion® consists of a hydrophobic polytetrafluoroethylene (PTFE)-like backbone and pendant chains with sulfonated ($SO_3{}^-$) end groups. Under humidified conditions, the hydrophilic end groups segregate into nano-sized clusters, which imbibe water and cause swelling. CLs with a Pt loading of 0.2 mg cm^{-2} (60 wt% Pt/C (P60K), Cataler, Japan) coated on a Teflon sheet (NITOFLON® Film, Nitto Denko, Japan) were transferred to both sides of the PEM using the heat press method at 3 MPa and 130 °C for 10 min. The corresponding CL was approximately 5 μm in thickness. Carbon paper (TGP-H-060, Toray) containing a microporous layer (MPL) on one side was used as the GDL on both the anode and cathode sides.

2.2. PEM and MEA properties

Dimensional changes of the PEMs and MEAs due to swelling were measured between hydration and dehydration states. Cuts of 50 mm × 50 mm were made for each sample, and the thicknesses were measured with a micrometer (Mitutoyo, Japan) at 23 °C and 50 RH%. The samples were soaked in de-ionized water at 80 °C or 50 °C for 2 h, and then the dimensions were measured. The samples were then dried at 80 °C or 50 °C for 1 h in an oven, which is dried in humidity below 5 RH%, and the dimensions were again measured. The dimension changes were repeatedly measured during both phases at these temperatures.

Stress–strain (S–S) curves of the samples were measured using a tensile testing machine with a temperature and humidity controlled chamber (Instron, USA). The samples were soaked at 80 °C at 80, 50 or 15 RH% for 2 h, and then the S–S curves were measured at a strain rate of 0.0139 s^{-1}.

2.3. Humidity cycle test of PEM and MEA

The PEMs and MEAs were exposed to humidity cycles using the apparatus shown in Fig. 3. The area of samples compressed with GDLs was 13 cm^2. The exterior of this area was placed between rubber gaskets. A single test cell with double channel-serpentine graphite flow fields was used. The land-to-channel of flow fields was 1 mm wide. A sample placed between two GDLs was compressed between the flow fields at 50 N, 100 N or 200 N. A gas supplying system fed nitrogen (N_2) through humidifiers set at a dew point of 80 °C and into the flow fields in the cell. Humidified N_2 and dry N_2 were alternately supplied to two side flow fields for 30 min. The flow rates were set at 0.5 L min^{-1} via a mass flow
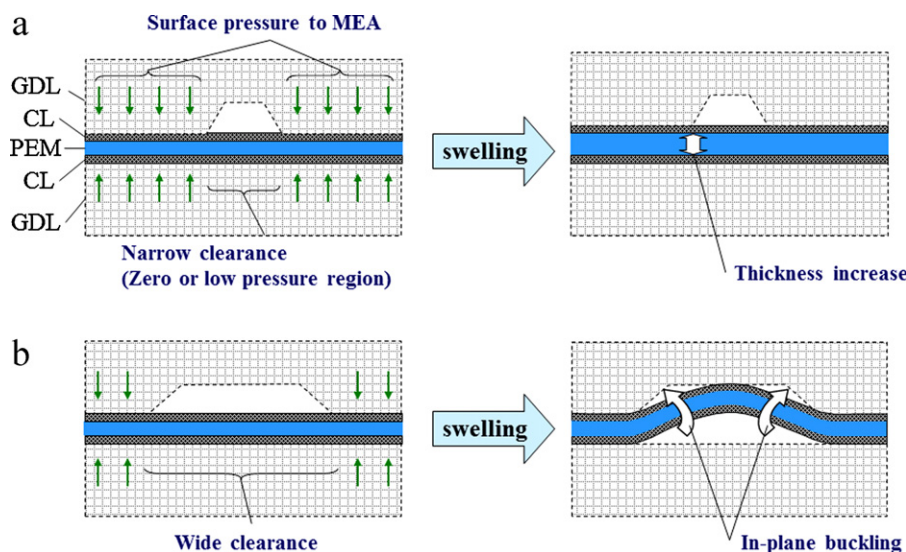

Fig. 2. Illustration of MEA deformations under clearances between the MEA and the GDL. (a) Thickness increase under narrow clearance and (b) in-plane buckling under wide clearance.
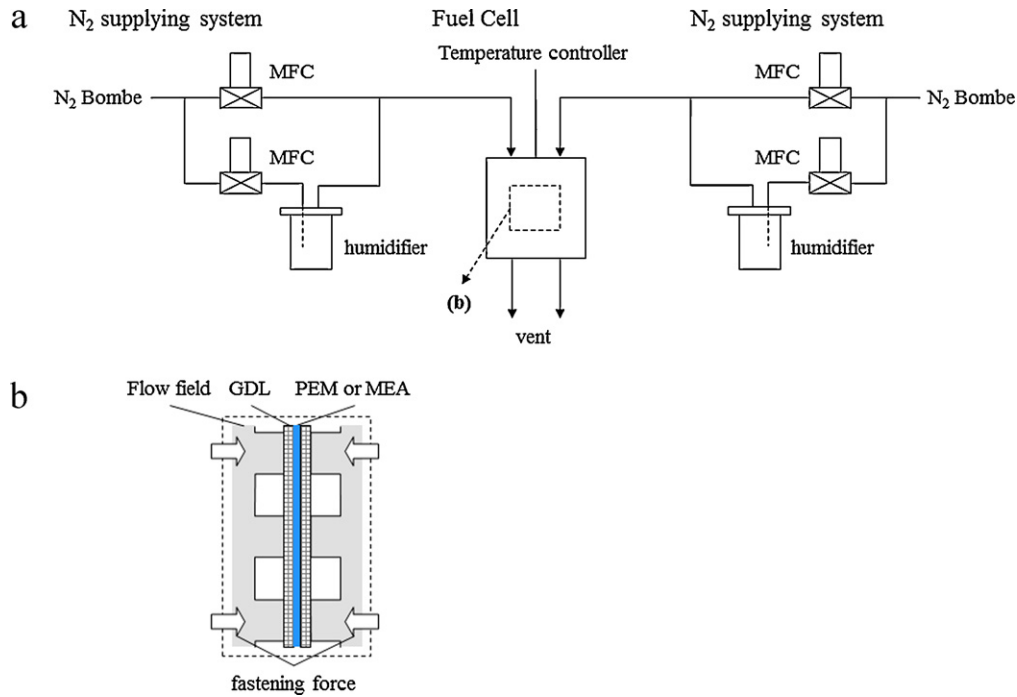
Fig. 3. (a) Illustration of the humidity cycle apparatus and (b) cross-section of the test cell.

controller (MFC). The humidity cycles were repeated 10 times. The PEM's water content profile was determined by measuring the high frequency resistance (HFR) of the cell using the A/C impedance method at a frequency of 1 kHz [2]. The HFR was compared to the measured PEM resistance data at various RHs. The estimated RHs of the PEM were 120 RH% for the humidified N$_2$ feed and 5 RH% for the dry N$_2$ feed. Note that the term "120 RH%" was conveniently used to describe humidity with 1.2 times more water vapor than the saturation state (100 RH%). After the humidity cycle test, the sample was removed from the GDLs and then observed with a digital microscope (VHX-100, KEYENCE, Japan).

2.4. PEM and MEA buckling test

Microscopic holes were fabricated in a 36 mm × 36 mm polyimide film (PI) by laser processing. Three types of PI films (200 μm thickness) were prepared. The adjusted diameters were 60–210 μm, 220–370 μm and 380–530 μm at every 10 μm (Fig. 4(a)). The term ϕ is defined as a symbol of a diameter. A film with ϕ 600 μm holes was also prepared. A hole of ϕ 200 μm was captured with SEM (VE-7800, Keyence, Japan) in Fig. 4(b). The diameter of each hole at the laser incidence side during fabrication was approximately 10 μm larger than that at the laser exit side, and the diameters at the incidence side were regulated at the designated size of ±2 μm.

The incidence side of the PI film was making contact with one side of the sample surface. The model test setup is shown in Fig. 4(c). A sample layered with a PI film was placed between two GDLs and was fastened with gas flow fields at 150 N. Humidity cycles were carried out in the same manner as the humidity cycle test, as noted in Section 2.3. The NRE212 deformation without humidity cycles was also examined. After the test, the sample was safely removed from the PI film and exposed to palladium sputtering. The specific region of the sample under the microscopic holes was captured by SEM. Subsequently, other portions were cut close to the center of the sample, perpendicular to the in-plane, with a razor blade, and observations were made from a side view.

The strain on the upside of the bulge was estimated by measuring the bulge length and bulge width in the SEM images. The bulge strain was then expressed using Eq. (1).

$$\text{bulge strain} = \frac{\text{bulge length} - \text{bulge width}}{\text{bulge width}} \tag{1}$$

The bulge strain with a clearance diameter change was quantitatively analyzed in each PEM and MEA.

3. Results

3.1. PEM and MEA properties

The dimensional changes of the PEMs and MEAs that occur after the PEMs and MEAs go through a 2nd hydration and dehydration phase are shown in Table 1. The dimensional changes of the NRE211 and NRE212 are similar. In the NRE212, the swelling ratio at 50 °C is approximately 70% of that at 80 °C. It is shown that the in-plane swelling ratio of the NRE211/CL and NRE212/CL decreases by more than 20% in comparison with the NRE211 and NRE212, respectively. With all samples, transverse direction (TD) swelling is slightly larger compared with machine direction (MD), and in-plane sizes decrease after dehydration. The swelling ratios in the thickness direction (ZD) tend to increase in comparison with the in-plane direction.

The engineering stress–strain curves of the PEMs and MEAs were measured in the MD of the PEM at 80 °C with 80, 50 or 15 RH%. The curves by 50% strain at 80 RH% or 15 RH% (partially) are shown in Fig. 5. The differences in stress are apparent for the PEM and MEA below 18% of strain. Moreover, the stress at 15 RH% is larger than that at 80 RH% in the NRE212 and NRE212/CL. Young's modulus was calculated at ~5% strain for each curve (Table 2). The data indicate that Young's modulus of the PEM increases by more than 15% when combined with CLs. Young's modulus shifts monotonically downward with an increase in humidity.
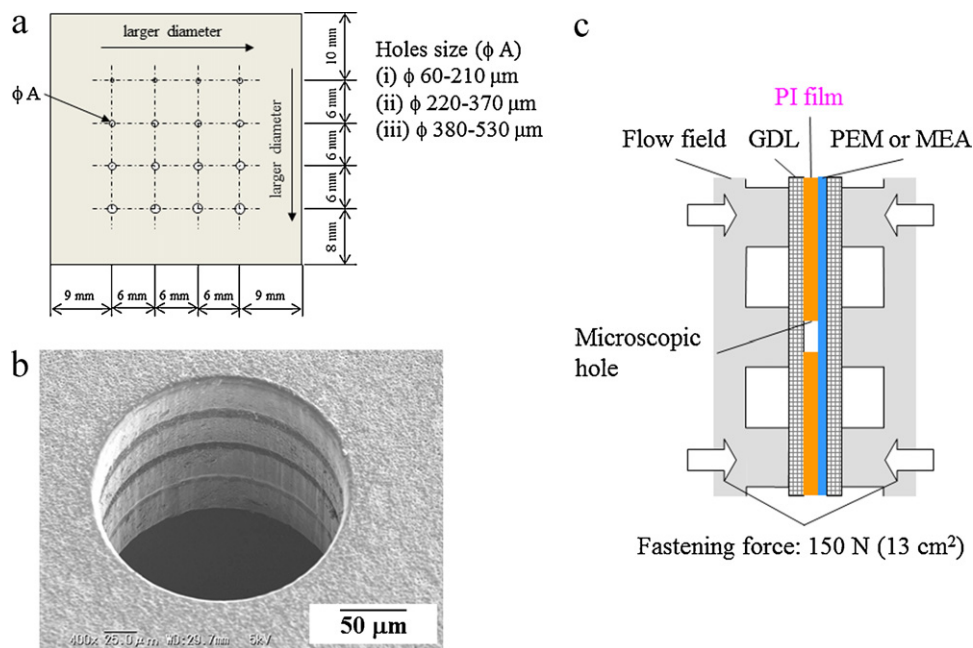
Fig. 4. (a) Polyimide film with16 microscopic holes, (b) SEM image of microscopic hole in the polyimide film at ϕ 200 μm, and (c) model test setup for the PEM and the MEA buckling under humidity cycles.

Table 1
Dimensional changes of PEMs and MEAs in hydration and dehydration.

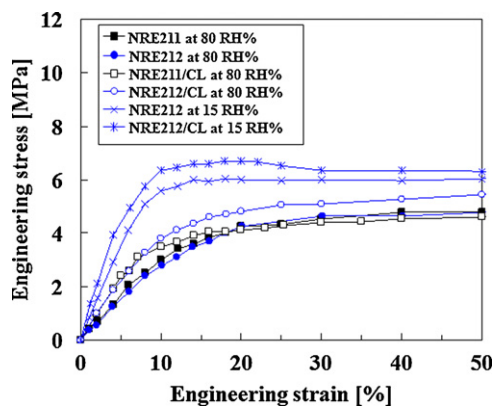| Sample	Initial thickness (μm)	Temperature (°C)	Dimensional changes					
			Hydration			Dehydration		
			MD	TD	ZD	MD	TD	ZD
NRE211	26.0	80	0.159	0.164	0.300	−0.021	−0.017	0.108
NRE212	53.4	50	0.112	0.118	0.110	−0.015	−0.012	−0.038
NRE212	53.4	80	0.164	0.167	0.263	−0.040	−0.034	0.046
NRE211/CL	35.8	80	0.112	0.123	0.207	−0.024	−0.024	−0.065
NRE212/CL	64.2	80	0.128	0.131	0.258	−0.032	−0.027	−0.003

Fig. 5. Engineering stress–strain curves of the PEM and the MEA at 80 °C.

Table 2
Young's modulus of PEMs and MEAs at 80 °C.

Sample	Young's modulus (MPa)		
	80 RH%	50 RH%	15 RH%
NRE211	36.9	56.2	77.1
NRE212	34.4	56.4	75.3
NRE211/CL	45.5	70.2	90.9
NRE212/CL	46.0	66.2	87.8

3.2. Humidity cycle test of PEM and MEA

Humidity cycle tests of the NRE212 at fastening forces of 50, 100 or 200 N were carried out. After the cycles, the surface of the NRE212 was observed with a digital microscope. The NRE212 deformations into a wrinkle shape are observed at 50 and 100 N. On the contrary, wrinkle deformation does not take place at 200 N.

The deformations of the NRE211, NRE212 and NRE212/CL at 50 N are shown in Fig. 6. A grid sheet was placed under the PEM to visualize the PEM wrinkle sharply. These samples deformed into wrinkle shapes. The wrinkle shapes of samples are composed with many continuous circles and ellipses. The ranges of the minimum wrinkle width are also shown in Fig. 6. The width of the NRE212 is wider than that of the NRE211. The NRE212/CL has a wider wave than the NRE212.

3.3. PEM and MEA buckling test

This section summarizes the deformations of each PEM and MEA with clearance diameters. Representative SEM images of the sample surface on the PI film side are shown in Figs. 7–11. The portions deforming to PI holes are located in the center of the SEM images. The deformed portion corresponds to the hole in the PI film. The relationship between the clearance diameter and the bulge strain of the PEM and MEA is summarized in Fig. 12.

The SEM images of the NRE211, captured from an oblique view, at the 80 °C test are shown in Fig. 7. A very small bulge emerges at ϕ
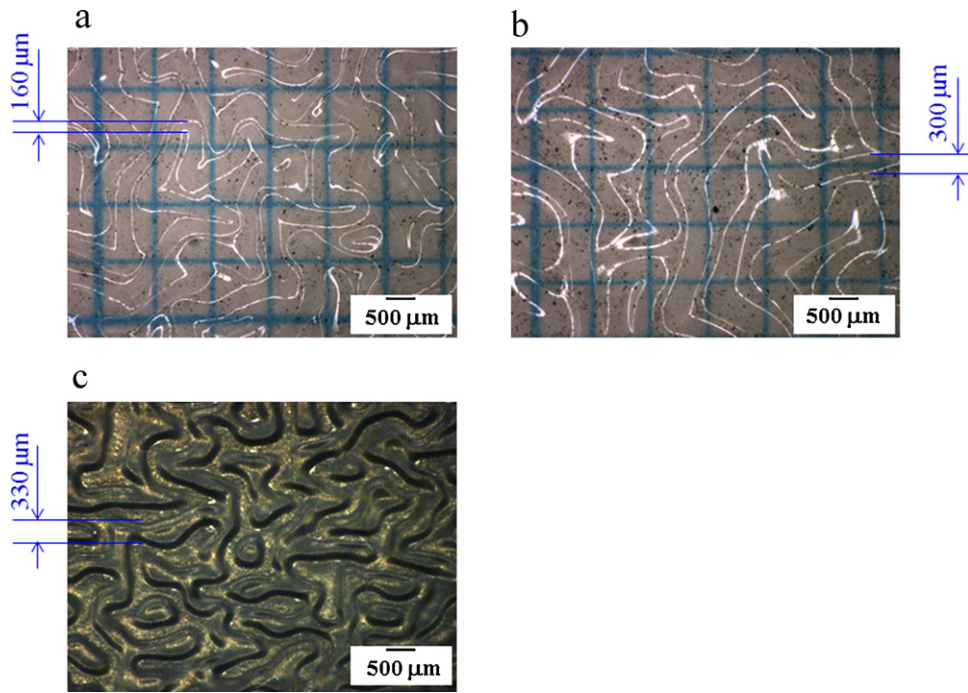
Fig. 6. Microscopic images of the PEM and the MEA deformations at 50 N after humidity cycles. (a) NRE211, (b) NRE212, and (c) NRE212/CL.

100 μm and increases with an increase in the clearance diameter. Moreover, the bulges become round at diameters above 140 μm. Fig. 12(a) indicates that the bulge strain dramatically increases at a diameter of 110 μm in the NRE211 at 80 °C.

The NRE212 deformations with the 50 °C test are shown in Fig. 8. Although slight bulges are found at φ 310 and 320 μm, a large bulge emerges at φ 330 μm. Fig. 12(a) shows a dramatic increase in the bulge strain at φ 330 μm.

The bulges are found at all clearance diameters in the NRE212 at the 80 °C test (figure is not shown). The bulge strains increase with an increase in the diameter, as shown in Fig. 12(a). The bulge strains significantly change at diameters ranging between 190 and 230 μm and highly expand at diameters above 240 μm.

The NRE212 bulges, cut through their center, are observed from a side view (Fig. 9). Although the upside slightly bulges, the downside does not yield to the upside at φ 150 μm. However, both sides bulge at φ 200 μm. The bulge is apparent at diameters above 300 μm, and the NRE212 is in a spherical and bending state.

The bulge strains of the MEAs with clearance diameters are shown in Fig. 12(b). In the NRE211/CL, small bulges occasionally emerge at diameters ranging between 200 and 260 μm. The bulge becomes larger at diameters above 270 μm. The deformations of the NRE212/CL are investigated as shown in Figs. 10 and 11, and at diameters ranging between 300 and 360 μm, the deformations change from flat form to a rounded. Figs. 10, 11 and 12(b) show remarkable bulges at diameters greater than 400 μm. The CL cracks perpendicular to the in-plane of the NRE212 are observed on the upside of the bulged surface at diameters above φ 500 μm in Figs. 10(f) and 11(c).
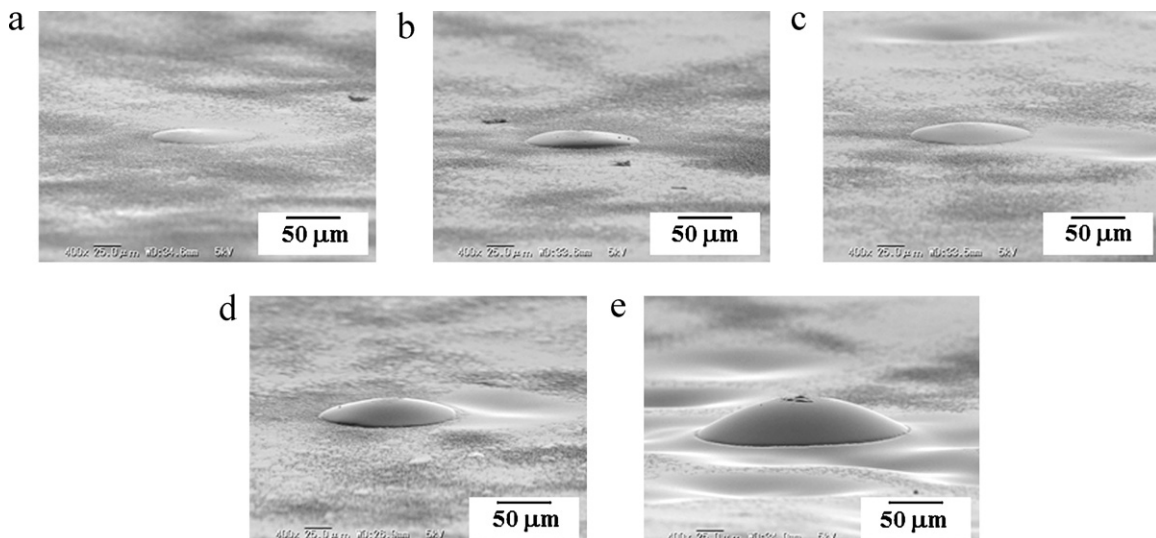

Fig. 7. SEM oblique-view images of NRE211 deformations at 80 °C to microscopic clearances. (a) φ 100 μm, (b) φ 110 μm, (c) φ 120 μm, (d) φ 140 μm, and (e) φ 210 μm.
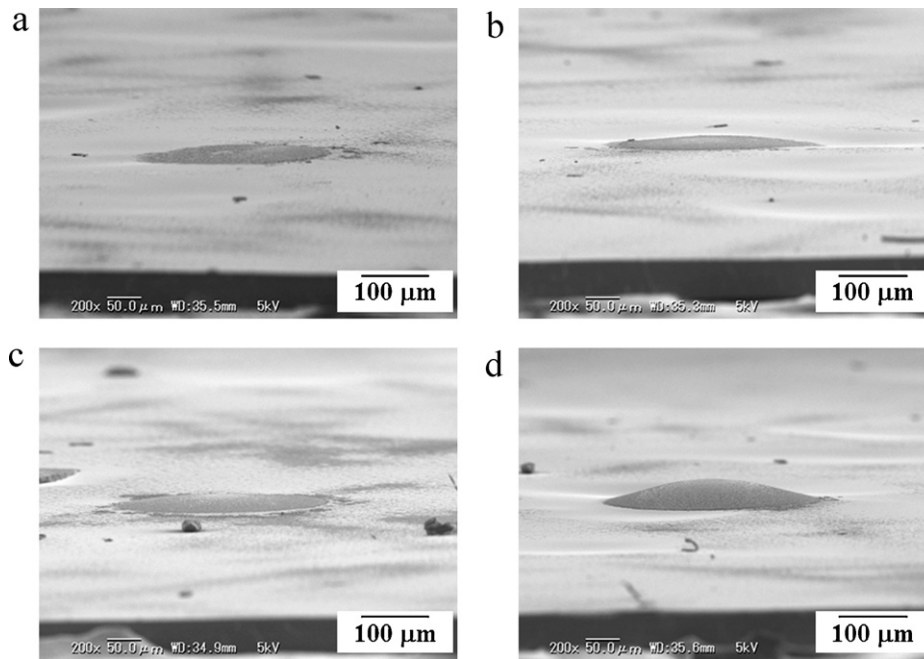
Fig. 8. SEM oblique-view images of NRE212 deformations at 50 °C to microscopic clearances. (a) φ 300 μm, (b) φ 310 μm, (c) φ 320 μm, and (d) φ 330 μm.

4. Discussion

4.1. PEM and MEA wrinkle deformations under humidity cycles

The PEM and MEA wrinkle deformations under humidity cycles, which were not attributed to sample shrinkage in the in-plane direction because the distance to the edges does not change, were examined. The samples are extended in the in-plane direction with permanent strain. This deformation can be understood by considering in-plane buckling under swelling. It is well known that compressive stress causes buckling in rods and plates. This buckling was studied in an elastic membrane [20–22], micromechanics [23], layered materials [24], membrane forming [25] and polymer gel swelling [26,27]. Compressive stress gives rise to buckling in any plate material when a critical stress is exceeded. A clamped plate will undergo buckling when the compressive stress exceeds the following critical stress (σ_{cr}) [20]

$$\sigma_{cr} = \frac{kE}{12(1 - \nu^2)} \left(\frac{t}{a} \right)^2 \tag{2}$$

where a is the half-width of the blister at the onset of buckling for a flat plate, t is the film thickness, and E and ν are the plate's Young's modulus and Poisson ratio, respectively. The term k is determined
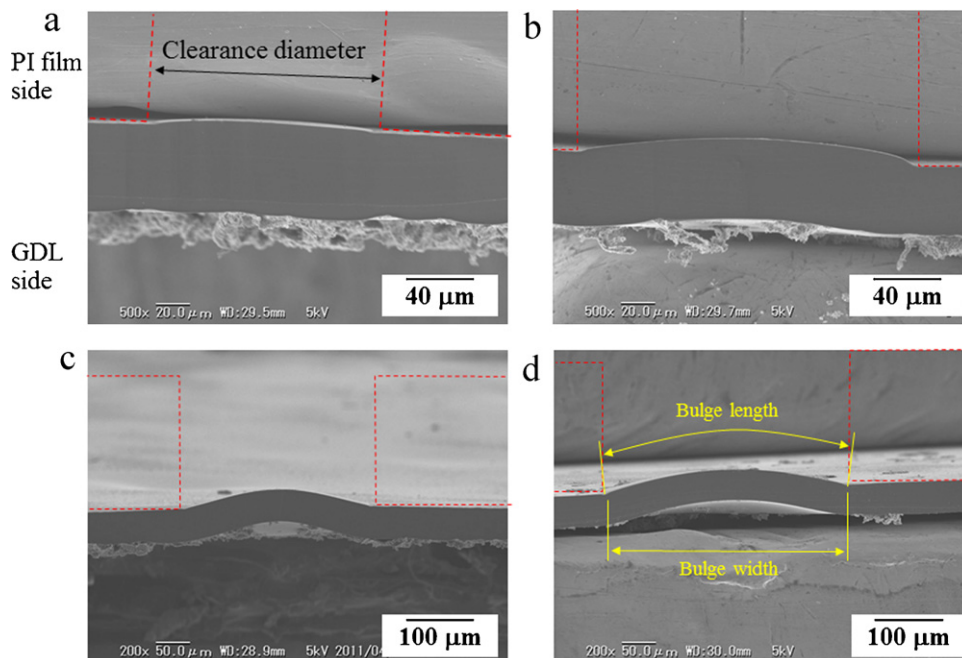

Fig. 9. SEM side-view images of NRE212 deformations at 80 °C to microscopic clearances. (a) φ 150 μm, (b) φ 200 μm, (c) φ 300 μm, and (d) φ 400 μm. Dotted-line indicates the position of the PI film during the buckling test.
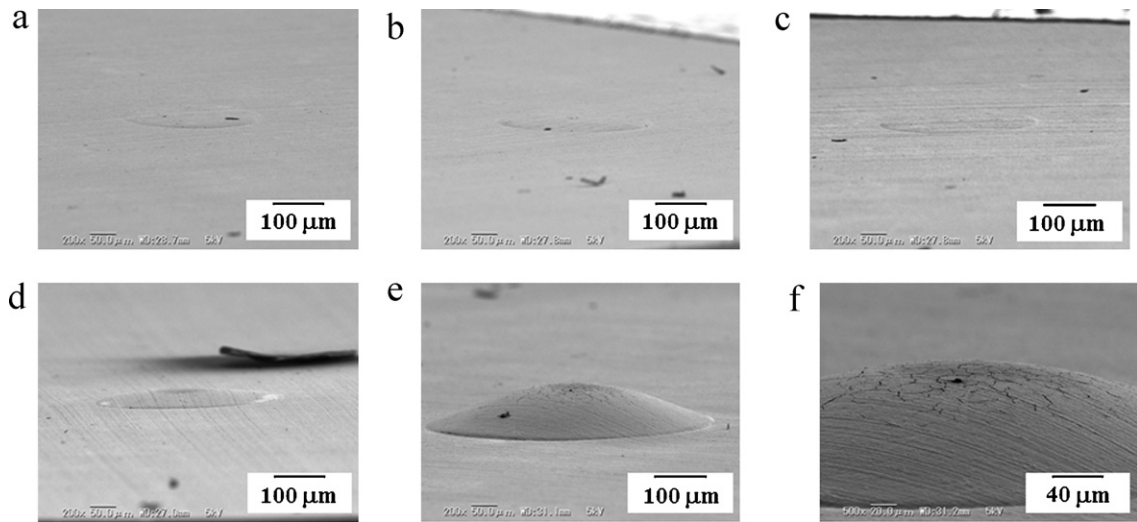
Fig. 10. SEM oblique-view images of NRE212/CL deformations at 80 °C to microscopic clearances. (a) φ 300 μm, (b) φ 320 μm, (c) φ 340 μm, (d) φ 400 μm, (e) φ 600 μm, and (f) CL cracks at φ 600 μm.
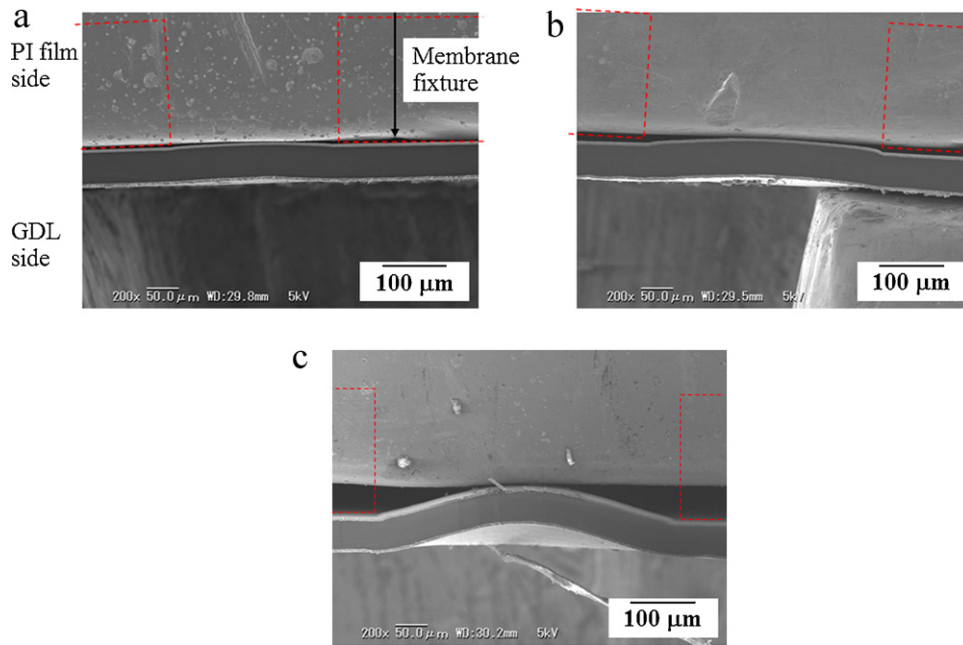

Fig. 11. SEM side-view images of NRE212/CL deformations at 80 °C to microscopic clearances. (a) φ 300 μm, (b) φ 400 μm, and (c) φ 500 μm. Dotted line indicates the position of the PI film during the buckling test.
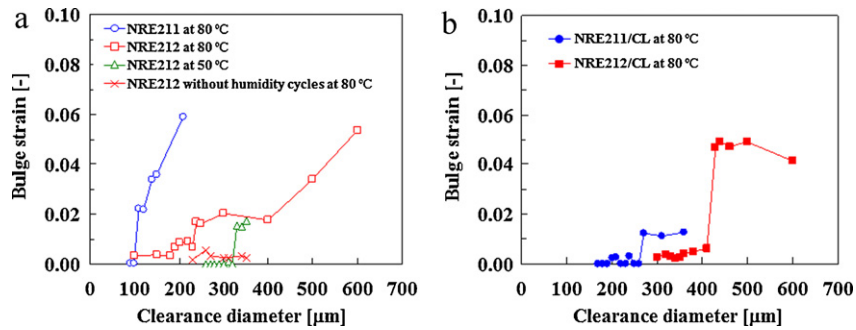

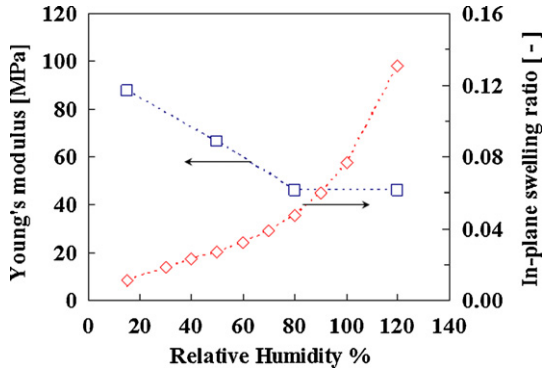**Fig. 12.** Bulge strain with a clearance diameter. (a) PEM and (b) MEA.

Fig. 13. Young's modulus and swelling ratio of NRE212/CL with relative humidity.

Fig. 14. Critical stress for buckling and compressive stress under swelling of NRE212/CL.

from the support condition of the plate and is 14.68 for the clamped circular plate.

A PEM expands with increases in both temperature and humidity. With the Dupont Nafion® persulfonic acid membrane [7,9–11,13,28,29], despite a thermal strain of approximately 1% with temperature changes of 100 °C [4], hygral strain under hydration (120 relative humidity (RH%)) is more than 15% [28]. Nafion® is hydrophilic in nature and swells in response to an increase in humidity. However, it swells almost twice as much in liquid water as in humid air at 90 RH% [9,28]. This water uptake phenomenon can be accounted for by Schroeder's paradox [29]. Swelling strain tends to increase at a higher temperature and in a more humid environment, as well as in liquid water [2,9,28]. At constrained in-plane deformations of the membrane, tensile or compressive stress is developed with changes in both temperature and humidity.

$$\sigma_{com} = \frac{E\varepsilon}{1-\nu} \tag{3}$$

where ε is the membrane in-plane strain with temperature and humidity changes when a dimensional change is not constrained. When the membrane is subjected to a hydration change, the compressive stress is developed in the membrane itself and causes buckling to the out-of-plane, which minimizes the systems elastic energy (Fig. 1). On the other hand, when the membrane is undergoing dehydration, a tensile stress is developed [2,4–10].

The possibility of NRE212/CL buckling under hydration can be verified by comparing the critical stress for buckling with the compressive stress under swelling. As shown in Fig. 6, the narrower width of the wave is 330 μm. The critical stress at a particular width can be calculated by Eq. (2) using the following properties of the NRE212/CL: $E = 46.0$ MPa (at 80 °C, 80 RH% in Table 2), $t = 64.2$ μm (in Table 1), $\nu = 0.4$ [11,12] and $2a = 330$ μm. Although Young's modulus for the Nafion® changes in correspondence with hydration changes, it is believed that Young's modulus at 80 RH% in water vapor should be similar to Young's modulus in liquid water at 80 °C [28]. Using these properties, the critical stress was estimated by Eq. (2) to be 10.1 MPa.

On the other hand, the compressive stress can be calculated using Eq. (3). Young's modulus and the in-plane swelling ratio are plotted against RH% in Fig. 13. Young's modulus at each RH% is interpolated linearly. The swelling ratio behavior is determined using the water content (λ) change based on the premise that the swelling is proportional to the polynomial equation of λ [9]. The swelling ratio at 120 RH% is 0.131 (in Table 1). Young's modulus and swelling ratio changes lead to the assumption that the compressive stress increases with an increasing RH% (Fig. 14). The compressive stress at 120 RH% was estimated to be 11.7 MPa. Increasing from 15 RH% to 120 RH%, despite a reduction in the Young's modulus by more than 50%, causes the swelling ratio to increase 10-fold. Therefore, the compressive stress increases along with the increase in RH%,
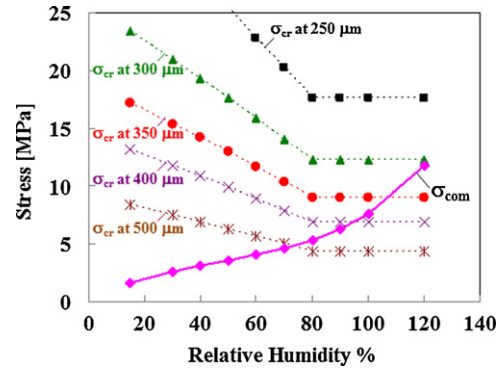
particularly during higher humidity while in the liquid state. It is concluded that the hydration can cause buckling of the NRE212/CL, due to the compressive stress exceeding the critical stress. These behaviors are also applied to the NRE211 and NRE212 based on these calculations and comparisons.

It is believed that a spherical shell is initially formed [20–22,24,26,27] when an isotropic compressive stress is present due to the property of Nafion® in which the isotropic stress nearly occurs (Table 1). When the compressive stress exceeds the critical stress during swelling, the surplus stress (the compressive stress minus the critical stress) is consumed in order to assist the MEA buckling into ellipses and continuous ellipses (worm-like patterns) [21,22]. Generally, the compressed membrane deforms into complex phase diagrams, which depend on the compressive stress and the stress anisotropy [21,22]. At a large isotropic compression of the MEA composed by Nafion®, the worm-like pattern is the state most conducive to releasing elastic energy. Different shapes would form in a PEM containing anisotropic swelling properties.

During hydration of the PEM, a permanent strain is developed within the wrinkled PEM and MEA. The wrinkle shape has been maintained after humidity cycles. On the other hand, buckling did not occur at a higher fastening force because the in-plane swelling ratio of the PEM under hydration was reduced [30].

4.2. Buckling condition for PEM and MEA

For the MEA and GDL, it is important, from an engineering design aspect, to know the buckling diameter corresponding to the membrane properties. By combining Eqs. (2) and (3), the minimum diameter for buckling ($2a_0$) at the circular membrane can be derived:

$$2a_0 = t\sqrt{\frac{k}{3(1+\nu)\varepsilon}} \tag{4}$$

The minimum diameter is proportional to t and inversely proportional to the square root of ε.

The PEM and MEA deformations into the defined clearance, after the humidity cycles, were analyzed. The estimated minimum diameters of PEMs and MEAs are listed in Table 3 and were compared against the actual minimum diameter, as calculated using Eq. (4). The thickness of samples at 25 °C and 50 RH% was adopted in these calculations. The calculation using a thinner thickness based on the dry conditions is effective for the initial phase of swelling. The in-plane swelling ratio of the TD is used in the calculation as well. PEMs freely absorb water and swell under PI holes because the PEM is not compressed along the thickness of the membrane.

It is important to notice that the bulges occur around the estimated minimum diameters. Moreover, bulge strains of the PEMs drastically increase around the estimated minimum diameter as

Sample	Temperature (°C)	In-plane swelling ratio	Estimated minimum diameter[a] (μm)
NRE211	80	0.164	120
NRE212	50	0.118	291
NRE212	80	0.167	244
NRE211/CL	80	0.123	191
NRE212/CL	80	0.131	332

[a] Estimated minimum diameter is calculated by Eq. (4).

Fig. 15. Relationship between the in-plane swelling ratio of MEA and the estimated minimum diameter for buckling with several MEA thicknesses.

shown in Fig. 12(a). The plastic deformation took place during the buckling. In the MEA, the bulges occurred around the estimated minimum diameter as well (Fig. 12(b)). However, the bulge strains remarkably increased at a diameter 50 μm larger than the estimated minimum diameter. In this region of the MEA, the bulge deformation under hydration is reduced corresponding to a comparative decrease in the in-plane swelling ratio. The CLs in this study are stiffer than the PEM due to the fact that Young' modulus of the MEA is larger than that of the PEM (Table 2).

The tests of the NRE211 at 80 °C (Fig. 7) and the NRE212 at 50 °C (Fig. 8) help determine the boundary value of the bulge occurrence during this experiment. On the contrary, small bulges at a lower clearance compared to the estimated minimum diameters were observed in the NRE212 at 80 °C (Fig. 9(a) and (b)) and NRE 212/CL (Figs. 10(a) and (b) and 11(a)). The primary characteristic of these bulges is that the upside is easily noticed in comparison with the downside. These bulges can arise from higher temperatures and thicker membranes and are not caused by in-plane buckling, but rather the plastic flow of the sample surface. The plastic flow occurred at higher temperatures with swelling along the thickness of the membrane present as well. Taking the NRE212 at 80 °C as an example, the bulge at diameters below 190 μm is the plastic flow due to the higher temperature. The additional bulge at diameters between 190 and 230 μm is the plastic flow due to the swelling along the thickness of the membrane. This consideration is supported by the NRE212 test without humidity cycles. The NRE212 was exposed to a temperature of 80 °C for 10 h without humidity cycles in the test cell. The bulge strains are not influenced by diameters between 230 and 350 μm. The bulge strain without humidity cycles (average strain of 0.003) is close to that at diameters ranging between 100 and 180 μm in the test with humidity cycles. Therefore, the bulge strains at diameters ranging between 100 and 180 μm are not influenced by the humidity cycles.

The PEM becomes less elastic at higher temperatures. The increase in thickness under swelling is larger in thicker samples. Therefore, the NRE212 and NRE212/CL at 80 °C tests tend to bulge into lower diameter clearances than the estimated minimum diameters.

4.3. Design guideline for preventing MEA buckling in fuel cells

The bulge expanded at larger clearance diameters (Figs. 7 and 9–11), and to explain this behavior, in-plane buckling during swelling was considered. Under fuel cell operations, the produced water is absorbed into PEMs. The RH% in the PEM is influenced by the generating condition. Fig. 14 plots the critical stress for buckling in the NRE212/CL along with the RH% change at each clearance diameter. The critical stress was calculated using Eq. (2) as previously explained. The compressive stress does not exceed the critical stress in the liquid state (120 RH%) at ϕ 300 μm, but the compressive stress does exceed the critical stress before 120 RH% (in water vapor) at diameters above 350 μm, and the NRE212/CL will therefore buckle. The surplus stress is consumed to assist expansion, and the NRE212/CL remarkably bulges as shown in Figs. 10(e) and 11(c). Thus, the bulge deformations of
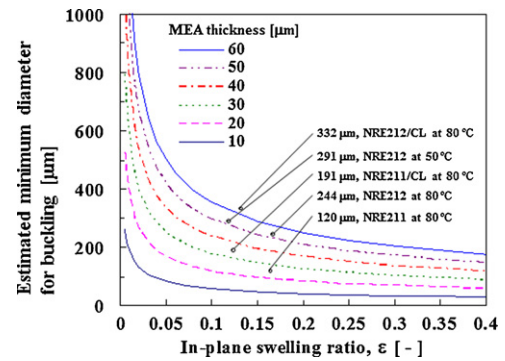
the NRE212/CL increase at larger clearance diameters. From these considerations, wider clearance between the MEA and GDL tend to cause plastic deformation after the in-plane buckling.

Surprisingly, the NRE211 bulges in the GDL surfaces can be observed in Fig. 7(c)–(e). Around the NRE211 bulge in the PI holes, round indents ranging between 150 and 200 μm in diameter were clarified. The PEM buckling tends to be of a plastic nature. In the MEA, the large CL cracks on the PEM and the delamination between the PEM and the CL can cause the PEM buckling.

In this study, the circular microscopic holes were used as the clearance, while the minimum diameter for buckling can be applied to the other clearance shapes. When the circle with the minimum diameter can fit into the existing clearance area, the membrane can deform into the clearance shape. The equation for estimation in each shape is listed in the reference literature [20].

The MEA buckling emerged in clearances at several hundreds of micrometers. This deformation is an initial mechanical degradation of the MEA. Although the buckling does not cause pinholes in the PEM immediately, it does cause locally large plastic strains. In Fig. 10(f), many CL cracks are observed on the upside of the MEA. Under dehydration of the PEM, the PEM is subjected to a tensile stress under the CL cracks [2,3,14]. By repeating humidity cycles, crazes would be initiated on the PEM under the CL cracks, resulting in pinhole formation in the PEM. Preventing the MEA from buckling is an effective mitigation method used to prolong MEA mechanical degradation.

Notice that Fig. 15 provides design guidelines for the MEA and GDL properties. The estimated minimum diameter against the in-plane swelling ratio and the MEA thickness can be easily estimated using Fig. 15. The buckling will be generated in clearances that are larger than each line. To prevent the MEA from buckling, several properties can be altered. The desirable properties in the PEM are a higher thickness and a lower in-plane swelling ratio. A reinforcement of the PEM effectively reduces the in-plane swelling [1,31]. Moreover, the desirable CL is thicker and rigid, which reduces in-plane swelling of the PEM. On the other hand, this paper points to a need for the development of a GDL surface with a lower roughness or both wider and lower clearances.

5. Conclusion

The present work is intended to investigate the mechanism of MEA wrinkle deformation under humidity cycles. The MEA, composed of the NRE212 and CL, deformed into a wrinkle shape under low fastening forces after humidity cycles. The wrinkle deformation was caused by in-plane buckling under swelling.

Next, an effort was devoted to clarify the mechanical design guidelines for the MEA and GDL to prevent MEA buckling. Clearances will occur in an interface between the MEA and the GDL.

The buckling tests of the PEM and MEA with different in-plane swelling ratios and thicknesses were carried out. The bulge strain of the PEM and MEA increased at the specific diameter, which is close to the estimated minimum diameter. The minimum clearance diameter was determined with the Euler in-plane buckling theory. The buckling test is very useful in examining buckling deformation, and the estimated minimum diameter is not only concise but also convenient for practical use. Reducing the in-plane swelling ratio is necessary to prevent MEA buckling. Additionally, the GDL with a flat surface allows the flexible design of PEMs dimensional change.

In the future, numerical analyses of the MEA under humidity cycles will be reported with identification of the MEA mechanical properties. Additionally, the mechanical degradation mechanisms of the MEA will be discussed.

Acknowledgments

References

[1] W.K. Liu, S.J.C. Cleghorn, B.E. Delaney, M. Crum, in: W. Vielstich, H.A. Gasteiger, H. Yokokawa (Eds.), Handbook of Fuel Cells, vol. 5: Advances in Electrocatalysis, Materials, Diagnostics and Durability, John Wiley & Sons, Ltd., 2009, pp. 385–402.
[2] Y.-H. Lai, D.A. Dillard, in: W. Vielstich, H.A. Gasteiger, H. Yokokawa (Eds.), Handbook of Fuel Cells, vol. 5: Advances in Electrocatalysis, Materials, Diagnostics and Durability, John Wiley & Sons, Ltd., 2009, pp. 403–419.
[3] M. Pestrak, Y. Li, S.W. Case, D.A. Dillard, M.W. Ellis, Y.-H. Lai, C.S. Gittleman, J. Fuel Cell Sci. Technol. 7 (2010), 041009-1–041009-10.
[4] A. Kusoglu, A.M. Karlsson, M.H. Santare, S. Cleghorn, W.B. Johnson, J. Power Sources 161 (2006) 987–996.
[5] A. Kusoglu, A.M. Karlsson, M.H. Santare, S. Cleghorn, W.B. Johnson, J. Power Sources 170 (2007) 345–358.
[6] A. Kusoglu, M.H. Santare, A.M. Karlsson, S. Cleghorn, W.B. Johnson, J. Electrochem. Soc. 157 (2010) B705–B713.
[7] R. Solasi, Y. Zou, X. Huang, K. Reifsnider, D. Condit, J. Power Sources 167 (2007) 366–377.
[8] W. Yoon, X. Huang, J. Electrochem. Soc. 157 (2010) B680–B690.
[9] Y.-H. Lai, C.K. Mittelsteadt, C.S. Gittleman, D.A. Dillard, J. Fuel Cell Sci. Technol. 6 (2009), 021002-1–021002-13.
[10] M.N. Silberstein, M.C. Boyce, J. Power Sources 196 (2011) 3452–3460.
[11] D.A. Dillard, Y. Li, J.R. Grohs, S.W. Case, M.W. Ellis, Y.-H. Lai, M.K. Budinski, C.S. Gittleman, J. Fuel Cell Sci. Technol. 6 (2009), 031014-1–031014-8.
[12] J.R. Grohs, Y. Li, D.A. Dillard, S.W. Case, M.W. Ellis, Y.-H. Lai, C.S. Gittleman, J. Power Sources 195 (2010) 527–531.
[13] Y. Li, D.A. Dillard, S.W. Case, M.W. Ellis, Y.-H. Lai, C.S. Gittleman, D.P. Miller, J. Power Sources 194 (2009) 873–879.
[14] T.T. Aindow, J. O'Neill, J. Power Sources 196 (2011) 3851–3854.
[15] I.-S. Park, W. Li, A. Manthiram, J. Power Sources 195 (2010) 7078–7082.
[16] Q. Guo, Z. Qi, J. Power Sources 160 (2006) 1269–1274.
[17] S. Kim, M.M. Mench, J. Power Sources 174 (2007) 206–220.
[18] Y.-H. Lai, Y. Li, J.A. Rock, J. Power Sources 195 (2010) 3215–3223.
[19] F.E. Hizir, S.O. Ural, E.C. Kumbur, M.M. Mench, J. Power Sources 195 (2010) 3463–3471.
[20] S.P. Timoshenko, J.M. Gere, Theory of Elastic Stability, second ed., McGraw Hill, New York, 1961.
[21] P. Peyla, Eur. Phys. J. B 48 (2005) 379–383.
[22] B. Audoly, B. Roman, A. Pocheau, Eur. Phys. J. B 27 (2002) 7–10.
[23] D.S. Popescu, T.S.J. Lammerink, M. Elwenspoek, Proc. IEEE MEMS Workshop, Oiso, Japan, 1994, pp. 188–192.
[24] A.G. Evans, J.W. Hutchinson, Int. J. Solids Struct. 20 (5) (1984) 455–466.
[25] P. Boisse, N. Hamila, E. Vidal-Salle, F. Dumont, Compos. Sci. Technol. 71 (2011) 683–692.
[26] T. Mora, A. Boudaoud, Eur. Phys. J. E 20 (2006) 119–124.
[27] Z. Liu, W. Hong, Z. Suo, S. Swaddiwudhipong, Y. Zhang, Comput. Mater. Sci. 49 (2010) S60–S64.
[28] A. Kusoglu, Y. Tang, M. Lugo, A.M. Karlsson, M.H. Santare, S. Cleghorn, W.B. Johnson, J. Power Sources 195 (2010) 483–492.
[29] A.Z. Weber, J. Newman, J. Electrochem. Soc. 150 (2003) A1008–A1015.
[30] J. Benziger, E. Chia, J.F. Moxley, I.G. Kevrekidis, Chem. Eng. Sci. 60 (2005) 1743–1759.
[31] Y. Tang, A. Kusoglu, A.M. Karlsson, M.H. Santare, S. Cleghorn, W.B. Johnson, J. Power Sources 175 (2008) 817–825.